Beam propagation near the dispersionless wavelength at 790 nm in rubidium

Hui Xia,[1,2,*] Christopher O'Brien,[2] Szymon Suckewer,[1] and Marlan O. Scully[1,2,3]

[1]*School of Engineering and Applied Science, Princeton University, Princeton, New Jersey 08542, USA*
[2]*The Institute for Quantum Science and Engineering, Texas A&M University, College Station, Texas 77843, USA*
[3]*Physics Department, Baylor University, Waco, Texas 76706, USA*

Between any two resonance lines for an atomic medium there exists a dispersionless wavelength where the ac Stark shift from the two resonances cancel and the real part of the resonant susceptibility is 0. We experimentally demonstrate the effects of this wavelength in a pump-probe experiment in high-density atomic vapor. A strong pump field excites the medium, in which we counterpropagate a broadband probe field. In a long cell, only at the dispersionless wavelength will scattering and self-focusing or defocusing not cause attenuation, allowing a spectrometer to read off the dispersionless wavelength. We perform a propagation experiment that shows the passband centered around the 790-nm dispersionless wavelength between the D_1 and the D_2 lines of rubidium.

I. INTRODUCTION

Between two resonances there is a point where the contributions to the ac Stark effect cancel each other, leaving a wavelength for which there is no resonant dispersion. Since when red detuned to a resonance there is positive resonant susceptibility, and when blue detuned to a resonance there is negative resonant susceptibility, it is clear that there must be a point where the resonant susceptibility is 0, a dispersionless point, as shown in Fig. 1. There is also a dispersionless point exactly on resonance, as the resonant refractive index switches sign, but this wavelength has strong absorption, making it less useful for many applications. These dispersionless wavelengths have been calculated for all alkali atoms [1,2], but only a few have been experimentally verified.

Since these dispersionless wavelengths are directly tied to the matrix elements of atomic transitions, measuring them helps check theoretical calculations of atomic structure [3]. Better knowledge of the matrix elements also helps improve uncertainties in atomic clocks [3,4]. These wavelengths can also be used for applications that require the ability to tune out the ac Stark shift, such as forming species-selective optical lattices [2]. It also has been suggested that the position of these dispersionless wavelengths can be controlled by applying magnetic fields to shift the frequency of the atomic energy levels in rubidium, in order to enable the easier generation of optical lattices [4].

But the most important application of these dispersionless wavelengths, we believe, is for the observation and control of collective effects. For example, a new technique for the generation of high-frequency light from low-frequency pumping using collective excitation and parametric difference frequency generation was recently suggested [5], where it is necessary to work at a point where the ac Stark effect can be neglected. Also, many experiments involving collective effects and multiple pulses struggle to have a long interaction region due to dispersion. Thus previous collective experiments, such as [6], were typically performed at resonance, sometimes utilizing a dense but subwavelength, thin layer of atoms

[7,8]. Working directly at resonance is not always desirable due to strong absorption of the applied fields. Therefore the dispersionless wavelengths are ideal for future experiments that rely on a long interaction region for collective excitation.

We develop an experimental technique to study and observe the effects of these dispersionless wavelengths on beam propagation in atomic vapor. A strong pump field excites the atomic medium, in which we counterpropagate a broadband probe field. The spatial (radial) intensity profile of the pump field leaves a spatially varying population as it travels through the cell. This spatially varying refractive index then acts as a graded index (GRIN) lens, for the counterpropagating probe field. Therefore, in a long gas cell, only at the dispersionless wavelength will the probe travel freely; at all other wavelengths the probe field will be focused or defocused. If a collection lens is placed in the near field, both focusing and defocusing will strongly attenuate the probe light that makes it to the detector. By propagating a broadband probe field, a spectrometer can read off the dispersionless wavelength. We use this technique to observe the dispersionless wavelength at 790 nm in rubidium vapor. We note that dispersionless wavelengths in rubidium were experimentally measured to a high precision using Bose-Einstein condensates (BECs) [3,9]; here we focus on the effects of dispersion on the beam propagation and window of free passage around this wavelength in hot and high-density rubidium vapor, and this technique can also be used for identifying dispersionless wavelengths in other atomic species that BEC-based interferometers are difficult to achieve.

First, we explain how the pump field creates a gradient refractive index lens, which focuses or defocuses any probe field that is not at the dispersionless wavelength. Then we explain how we perform the experiment to detect the dispersionless wavelength at 790 nm, between the D_1 and the D_2 resonances of rubidium, and present the results. Finally, we discuss some applications and implications for the dispersionless 790 nm, in particular, how this frequency is ideal for observing collective effects in atomic vapor.

II. GRADED INDEX LENS

Between two resonance lines is a 0 in the resonant susceptibility. This is demonstrated in Fig. 1. At this dispersionless

*hxia@princeton.edu
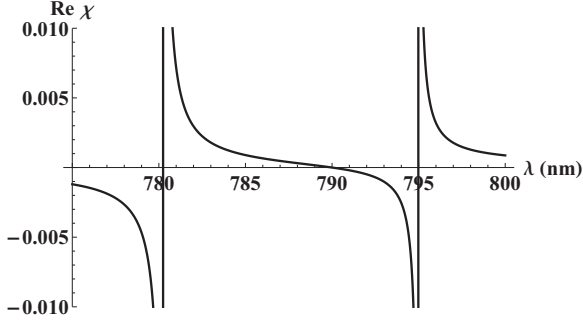
FIG. 1. Resonant susceptibility as a function of laser wavelength for a natural abundance of rubidium, at a temperature of $250\,°C$. The real part of the resonant susceptibility goes through 0 at the two transition wavelengths and at the dispersionless wavelength at 790 nm.

wavelength, not only is there no resonant dispersion, but the ac Stark effects from each transition cancel.

Here we are particularly interested in the dispersionless wavelength between the D_1 and the D_2 lines of rubidium at 790 nm [2]. For a probe field of linear polarization, we can treat the rubidium as a superposition of two two-level atomic responses, one for the D_1 line and one for the D_2 line. In the absence of a pump field, the resonant susceptibility as a function of the probe frequency can be expressed as [10]

$$\chi(\omega) = \frac{N}{\epsilon_0 \hbar}\left(\frac{\mu_{D1}^2}{\omega_{D1} - \omega - i\gamma_{D1}} + \frac{\mu_{D2}^2}{\omega_{D2} - \omega - i\gamma_{D2}}\right), \quad (1)$$

where N is the rubidium density, ω is the probe frequency, μ_{D1} and μ_{D2} are the dipole matrix elements, ω_{D1} and ω_{D2} are the transition frequencies, and γ_{D1} and γ_{D2} are the total transition linewidths for the D_1 and D_2 lines. Using Racah algebra for matrix elements involving coupled angular momentum states [11], the ratio between μ_{D2}^2 an μ_{D1}^2 can be calculated to be 2; higher precision calculations can be found in [12]. There exists a frequency ω, between ω_{D1} and ω_{D2}, such that the contributions from D_1 and D_2 cancel and $\chi(\omega)$ is 0 at that frequency, which for rubidium happens at 790 nm. For a circularly polarized probe field, the calculation of susceptibility involves more states. Yet due to the correlations among the matrix elements of rubidium D_1 and D_2 lines, as long as the population is initially evenly distributed among the spin levels of the ground state, contributions from D_1 and D_2 transitions have the same ratio as in the case of the linearly polarized probe, therefore the dispersionless wavelength calculated for linear polarization from Eq. (1) is also valid in the case of the circularly polarized probe field.

In Eq. (1), we have also assumed that all the atoms are in the ground state. In the presence of the pump field, a fraction of the population will be excited to upper states, and the susceptibility seen by the probe field will be modified to

$$\chi(\omega) = \frac{N}{\epsilon_0 \hbar}\left[\frac{\mu_{D1}^2\left(\rho_g - \rho_e^{D1}\right)}{\omega_{D1} - \omega - i\gamma_{D1}} + \frac{\mu_{D2}^2\left(\rho_g - \rho_e^{D2}\right)}{\omega_{D2} - \omega - i\gamma_{D2}}\right], \quad (2)$$

where the terms $\rho_g - \rho_e^{D1}$ and $\rho_g - \rho_e^{D2}$ represent the population difference between ground and excited states. If the probe frequency is away from the dispersionless wavelength,

the D_1 and D_2 terms in brackets in Eq. (2) will not cancel and the susceptibility depends on the population distribution and, thus, can spatially vary due to the radial variation of the pump field.

Starting with the exact time-domain solution of the density matrix for a two-level atom [13], we can calculate the average difference in population between the ground and the excited states in the presence of a pump field,

$$\rho_g - \rho_e = 1 - \frac{|\Omega|^2}{|\Omega|^2 + \Delta^2}, \quad (3)$$

where $\Omega = \vec{d}\cdot\vec{E}/\hbar$ is the Rabi frequency of the pump, while $\Delta = \omega_p - \omega_0$ is the detuning of the transition frequency ω_0 from the pump laser frequency ω_p. We assume a pump field strong enough to saturate the transition on resonance, thus we take $|\Omega| \gg \gamma$. The pump field propagating through the medium has a radial intensity profile, which causes a radial distribution of the Rabi frequency and thus the atomic population. This causes a radial distribution of the resonant susceptibility. Along the length of the cell the amount of absorption of the pump field is less than 1%, and for simplicity we neglect the self-focusing or defocusing of the pump, so there is no significant z dependence of the susceptibility.

When the probe field propagates through the medium the presence of the radially distributed resonant susceptibility creates a GRIN lens, where instead of having a curved interface between two different refractive index materials, there is a gradual change in the refractive index that, nevertheless, still behaves similarly to a classical lens. The radial profile of refractive index for probe wavelengths where the resonant susceptibility is positive creates a defocusing lens since at the center of the beam the population is saturated and thus smaller than at the edges. In the radial profile for the probe wavelengths with negative resonant susceptibility a focusing lens is created since at the center of the beam the refractive index is higher. However, when the susceptibility is 0 at the dispersionless wavelength, the light is allowed to travel unimpeded to the detector. If the population differences between the excited states of D_1 and D_2 transitions can be neglected (i.e., assuming $\rho_e^{D1} = \rho_e^{D2}$), the dispersionless wavelength remains at the same position as in the case of no pump [Eq. (1)]. If the difference between ρ_e^{D1} and ρ_e^{D2} is taken into account, the dispersionless wavelength itself can also shift slightly from the zero-crossing position predicted by Eq. (1) and have a spatial dependence determined by the radial intensity profile of the pump. However, in cases where the pump field transfers the ground-state population to states other than the states of D_1 and D_2 lines (for example, to the 5^2D level via two-photon transition), the assumption of $\rho_e^{D1} = \rho_e^{D2}$ is sufficiently accurate (they both can be considered 0) and only ρ_g shows spatial dependence on the radial profile of the pump beam, therefore the D_1 and D_2 terms in Eq. (2) will cancel at the same dispersionless wavelength as in Eq. (1).

Propagation of the probe beam can be understood by studying ray tracing of the beam through the GRIN. This is done by solving the ray equation,

$$\frac{d}{ds}\left(n(\vec{r})\frac{d\vec{r}}{ds}\right) = \nabla n(\vec{r}), \quad (4)$$
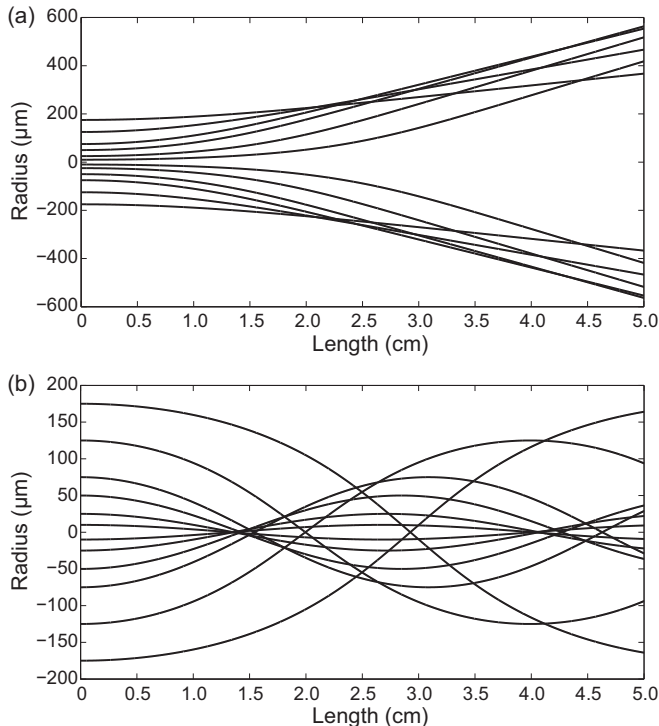
FIG. 2. Ray tracing plots for a probe laser of diameter 250 μm propagating through 5 cm of the medium where the refractive index difference Δn (compared to the area outside the pumped region) is uniform along the propagation axis and distributed as a Gaussian in the radial direction with a full width at half-maximum of 400 μm, which we use to model the distribution due to the pump laser. Here we choose refractive index changes to be similar to those in experiments. (a) The peak refractive index difference is taken as $\Delta n_{max} = -0.0001$, which creates a defocusing gradient refractive index lens. (b) The peak refractive index difference is taken as $\Delta n_{max} = +0.0001$, which creates a focusing gradient refractive index lens.

where $\vec{r}$ is the position vector of a point along the ray, ds is the element of arc length along the ray, and $n(\vec{r})$ is the radially varying refractive index distribution. Using the method of ray tracing given in [14] we plot the effects of a defocusing lens and focusing lens in Fig. 2.

III. PROPAGATION EXPERIMENT

We performed pump-probe experiments in high-density rubidium vapor. A natural abundance of rubidium is preloaded in a 2.5-cm-diameter and 5-cm-long Pyrex cell without buffer gas. The cell is heated to temperatures near 200–250 °C to reach a Rb density at levels of 10^{15} cm^{-3}. Two Ti:sapphire laser systems provide the pump and probe pulses at a repetition rate of 10 Hz. The pump system consists of a regenerative Ti:sapphire amplifier seeded by a tunable cw Ti:sapphire oscillator. The pump beam has a typical energy of 0.5 to 1 mJ, a pulse duration of 18 ns, and a linewidth of 0.1 nm and can be tuned from 765 to 805 nm. The pump laser is multi-longitudinal-mode, with a mode spacing of 2×10^{-4} nm, therefore, about 500 modes are contained within the linewidth of the pump field. At a total pump intensity of the order of 10^7 W/cm^2, the Rabi frequency of each mode is about

6×10^{10} s^{-1} for exciting the $5S$-$5P_{3/2}$ transition of rubidium, which is significantly less than the typical detuning of the pump field from the $5S$-$5P_{3/2}$ resonance (about 3×10^{12} s^{-1} for each 1 nm of detuning). Equation (3) can be used to estimate the population excited by each mode of the pump, and the total excitation is the sum for all the modes. The probe laser can be operated either as a narrow-band (linewidth < 0.1 nm) pulse tunable from 765 to 805 nm, or as a broadband pulse having a spectrum covering the range of 770–810 nm. The probe has a pulse duration of 15 ns, and the energy of the probe pulse is attenuated to the order of 30 nJ before entering the cell. The timing of both pump and probe pulses are controlled by intracavity Pockel cells in each system and the two systems are synchronized by digital delay generators from Stanford Research Systems (SRS). Both beams are linearly polarized and the relative delay between the pump-probe pulses is controlled by varying the Pockel cell timing.

To observe the effects of the GRIN formed by rubidium under a near-resonance pump, we compare CCD images of the spatial profile of the probe beam after it passes through the cell, as shown in Fig. 3. In these data, the probe has a bandwidth of less than 0.03 nm. The pump laser counterpropagates with the probe. The pump and probe are focused on the cell center and both beams have diameters of 0.8 mm. The CCD is positioned 55 cm after the cell, within the Rayleigh range of the probe. Without the pump, the probe beam profiles (left column in Fig. 3) look very similar to each other; in fact they are all similar to the patterns when the cell is cold. However, the presence of the pump leads to a radially dependent phase shift on the probe, effectively forming a positive or negative lens depending on the probe wavelength, as shown in Figs. 3(b) and 3(f), except for the case where the probe is near 790 nm, i.e., Fig. 3(d). In the vicinity of 790 nm, the phase shift due to rubidium is nearly 0 to start with, and the pump beam will not cause any spatially dependent phase shift on the probe; the spatial profile of the beam pattern is preserved.

The dispersionless wavelength of rubidium can also be observed with a broadband probe together with a spectrometer. As shown in Fig. 4(a), the probe is focused on the cell and the transmitted probe spectrum is recorded by a 0.5-m spectrometer positioned 90 cm after the cell. The spectral resolution of the spectrometer is 0.15 nm at a wavelength of 800 nm. At the cell center, the diameter of the probe beam is 250 μm. The counterpropagating pump beam is focused on the cell at a diameter of 400 μm and a peak intensity of 2–3 $\times 10^7$ W/cm^2. A collection lens is used after the cell to image the probe beam onto the slit of the spectrometer. Figure 4(b) shows transmitted spectrum of a broadband probe at a cell temperature of 250 °C, with and without a pump pulse. In the absence of the pump, rubidium absorption corresponding to the $5S$-$5P_{1/2}$ (795-nm) and $5S$-$5P_{3/2}$ (780-nm) transitions is shown as dips in the probe spectrum. The measured spectrum is a convolution of the real spectrum of a transmitted probe with a window function whose width is determined by the resolution of the spectrometer, so the width and depth of the absorption dips are limited by the spectrometer resolution at lower temperatures (densities) until the width of the Voight profile of the absorption spectrum exceeds the spectrometer resolution.

In the presence of a 775-nm and 2.5×10^7 W/cm^2 pump pulse, the probe beam has good transmission only near the
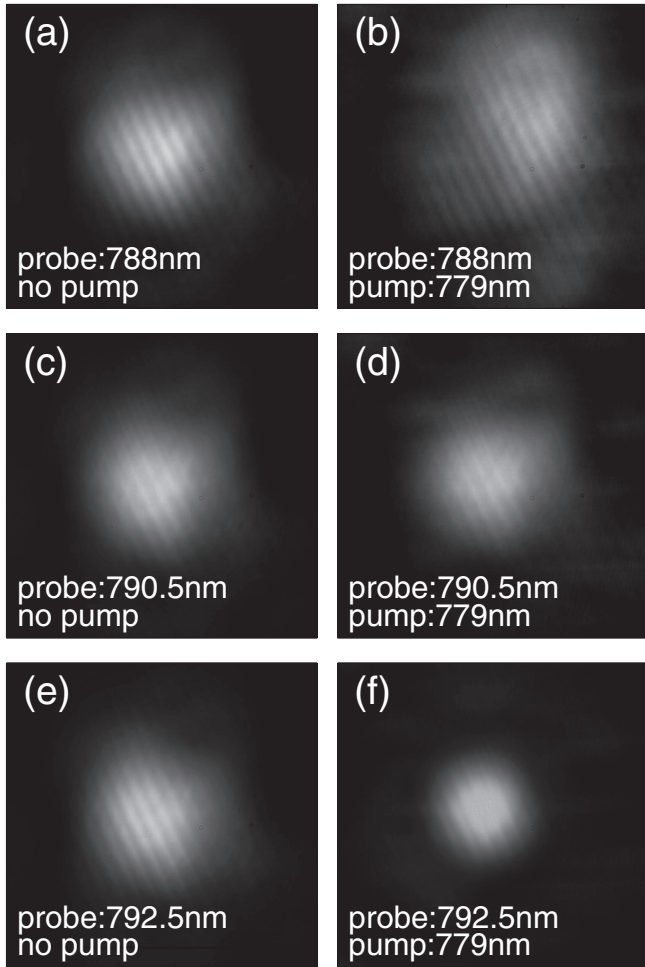
FIG. 3. CCD images of the spatial profile of a narrow-bandwidth probe beam after passing through the rubidium cell. In the presence of the pump, the rubidium vapor behaves as a positive or negative lens seen by the probe field, leading to focusing or defocusing, except at the dispersionless wavelength. For these data, the cell is at the temperature of 230 °C. The pump has an intensity of 6×10^6 W/cm^2 and counter-propagates with the probe. Both the pump and the probe are focused on the cell center and have diameters of 0.8 mm.

FIG. 4. (a) Experimental setup showing the forward-propagating pump field and backward-propagating probe field. (b) Transmitted spectra of the probe pulse with (blue) or without (red) the pump pulse. For these data, the cell is heated to 250 °C, the pump is at 775 nm, and the intensity is 2.5×10^7 W/cm^2. The absorption of rubidium is shown as the dips at wavelengths corresponding to $5S$-$5P_{1/2}$ (795-nm) and $5S$-$5P_{3/2}$ (780-nm) transitions. The narrow line at 775 nm in the spectrum in presence of pump is the back reflection of the pump beam from several sources including stray reflections or scattering due to cell window and mirrors.

region of 790 nm. It should be emphasized that, in our detection scheme, the recorded spectra represent the fluence (i.e., energy per unit area) instead of the total energy of each frequency component in the probe beam at the position of the spectrometer entrance slit (30 μm wide). If any frequency component has a relatively different spatial distribution profile after propagating through the rubidium vapor, it will lead to a change in the spectrum recorded by the spectrometer, even if the total energy of this frequency component over the whole beam area remains unchanged. Therefore, the spectrum is influenced not only by the absorption or amplification, which is related to the imaginary part of the susceptibility of the medium, but also by the alteration of the phase front, which is related to the refractive index or real part of the susceptibility. The extra (wavelength-dependent) focusing or defocusing caused by the rubidium on the probe will alter the imaging geometry of the collection lens after the cell, therefore reducing the amount of light entering the slit of the

spectrometer for the corresponding wavelength component in the broadband probe.

Figure 5 shows transmitted probe spectra under different cell and pump conditions. The evolution of the spectra at different pump-probe delay times in Fig. 5(a) shows that the effects of the pump on the probe spectrum can last at least a few microseconds. The reason this is much longer than the spontaneous decay time of the $5P_{1/2}$ or $5P_{3/2}$ level is, we believe, due to the radiation trapping effects in the high-density rubidium vapor. In high-density atomic vapors, each emitted photon from an excited atom can be reabsorbed and reemitted repeatedly by other atoms; as a result of this "radiation trapping" effect, the effective radiative decay rate of a resonance line can be significantly decreased. The effective radiative rate is often described as the natural decay rate multiplied by an escape factor g, which is the inverse of the mean number of absorption events. For simplicity, we adopt the approximate formulation for the escape factor in [15] to have an order-of-magnitude estimate. Assuming conditions of a Doppler broadened line, high opacity, and uniformly distributed excited-state atoms in a geometry of
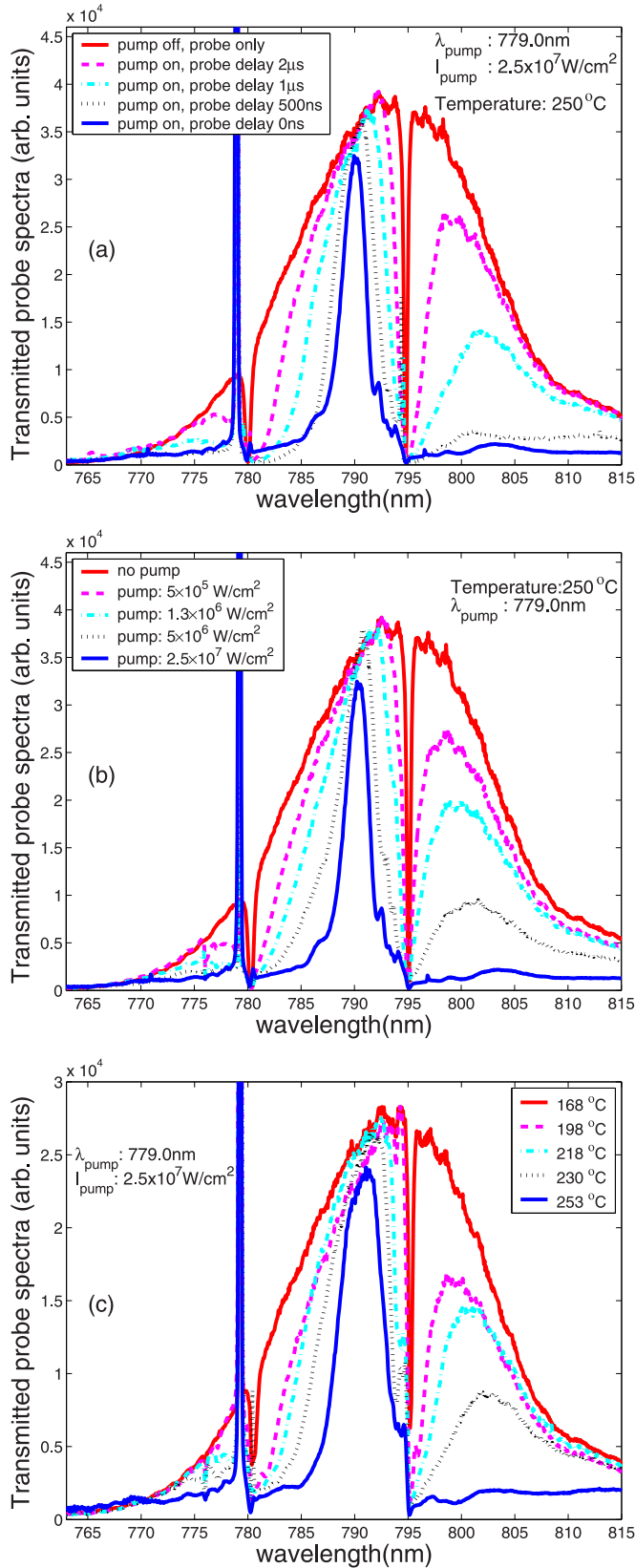
FIG. 5. Transmitted probe spectra (a) at different delays after the pump pulse, (b) at different pump intensities, and (c) at different cell temperatures. For these data, the rubidium cell is 5 cm long.

infinite cylinder, the escape factor can be approximated as [15]

$$g = \frac{2}{\sqrt{\pi}} \frac{\sqrt{\ln(\alpha_0 R)}}{\alpha_0 R}, \tag{5}$$

where α_0 is the absorption coefficient at the line center and R is the radius of the cylinder containing the excited atoms, here in our case is the radius of the pump beam ($R = 200\ \mu$m). Under conditions of our experiment, the Doppler width is 0.7 GHz for the $5S$-$5P_{3/2}$ transition at $T = 250\,^\circ$C, and $\alpha_0 R$ is of the order of 10^3, the corresponding escape factor is about 10^{-3}. That is, the estimated effective decay time is 3 orders of magnitude longer than the natural decay time (26 ns). The diffusion of atoms is not included in the above simplified estimate. At a cell temperature of $250\,^\circ$C, the thermal transit time of atoms across the pumped region (defined by a pump beam diameter of 400 μm) is also at the microsecond level. Therefore, the dominating time constant observed experimentally here may be a combination of the thermal transit time through the active region and the delayed population decay under radiation trapping.

Figures 5(b) and 5(c) display the probe spectra at different pump intensities and cell temperatures. At lower pump intensities or cell temperatures (which means lower rubidium vapor densities), the "passband" near 790 nm widens and approaches that in the case where there is no pump. This is in agreement with the fact that the GRIN lens is weaker with either a lower pump intensity or a lower vapor density. The width and shape of the passband are dependent on the imaging setup for the probe beam from the cell center to the spectrometer entrance slit and also on the optical alignment between probe and pump beam, which could lead to variations in different runs. For example, in Fig. 5(c) the plot for $T = 253\,^\circ$C shows a similar main feature, a passband near 790 nm, as the curve for pump intensity 2.5×10^7 W/cm^2 in Fig. 5(b), but the actual width and shape are slightly different, even though the cell temperature and pump intensity are similar; this is due to the drift of the spatial mode profile of the probe beam and its alignment with the pump beam.

IV. DISCUSSION

Both the spatial profile and the spectroscopy measurements of the probe have demonstrated the effects of the GRIN induced by the strong pump field. The probe field travels freely through the medium only near the dispersionless wavelength since only there does the GRIN effect not occur. The same would happen at resonance, but there the absorption is too strong for the probe to travel through the medium. Similar effects could be realized from having a coherent grating in the medium, but for a coherent grating to exist, it has been shown that the coherence time of the medium needs to be longer than the pulse length [6]. For rubidium vapor at $250\,^\circ$C, with a density of 4×10^{15} cm^{-3}, the collisional broadening for the D_1 or D_2 lines can be estimated to be around 0.2 GHz [10], which means the collisional effects alone would limit the coherence time to around 2 ns or less, almost an order of magnitude shorter than the pump pulse length (18 ns). This was also demonstrated by changing the delay time between the pump and the probe field, which showed that the effect
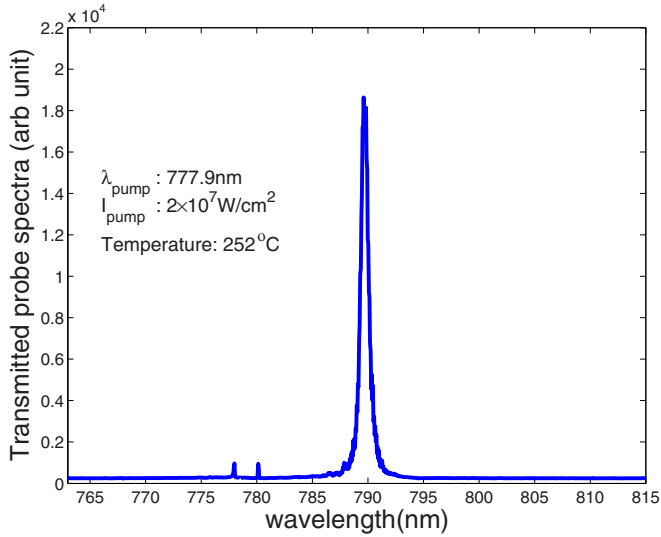
FIG. 6. The transmitted probe spectrum has an FWHM width of 0.8 nm with a 10-cm-long rubidium cell, heated to $252\,^\circ$C (rubidium density of 5×10^{15} cm^{-3}). The pump laser has an intensity of 2×10^7 W/cm^2 and is tuned to 777.9 nm (in the vicinity of the two-photon resonance for the $5S$-5^2D transition). The resolution of the spectrometer is 0.15 nm at a wavelength of 800 nm.

remains until delays of microseconds, which are much longer than the coherence time and similar to the time it takes the population distribution to diffuse, as expected with the GRIN effect. It is also possible for the signal to be reflecting off of a spatially varying refractive index, or "population grating." Such a population grating would form along the axis from the back reflection of the pump field, but that can be ruled out since the glass at the cell exit is angled at 5°, which, when combined with the low, 4% reflection off uncoated glass, does not give a strong enough reflection to cause a population grating to form in the cell.

This experiment can be used to find the dispersionless wavelength between two transitions, which can be useful for measuring the matrix elements of transitions, but as shown in Fig. 4 the spectrum of the transmitted pulse is not narrow enough for precise measurement. A longer cell and optimized detection geometry can improve the precision to a certain extent, as shown in Fig. 6; the transmitted probe spectrum has an FWHM of 0.8 nm with a cell 10 cm long heated to $252\,^\circ$C and a 0.5-m spectrometer with a line CCD detector array. The pump laser is also tuned to the vicinity

of the two-photon resonance for the $5S$-5^2D transition. Our observations have shown that when the pump laser is tuned closer to the two-photon resonance of the $5S$-5^2D transition, the passband also gets narrower, which indicates a stronger lens effect as a larger portion of the population is transferred from the ground state to the 5^2D level. On the other hand, if the pump is tuned to one-photon resonance of the D_1 or D_2 transition, i.e., $5S$-$5P_{1/2}$ (795 nm) or $5S$-$5P_{3/2}$ (780 nm), the shape of the passband may get distorted and the peak wavelength (dispersionless wavelength) will also shift since the population difference between the $5P_{1/2}$ and the $5P_{3/2}$ levels resulting from the population transfer by the pump is significant enough to shift the dispersion curve.

The dispersionless wavelength has useful implications for the study of coherence and collective effects in field propagation. Since at these wavelengths self-focusing is negligible and the dispersion is uniform, these points could be useful for collective experiments. For this reason, studying the propagation of intense pulses near the dispersionless wavelength is important.

V. CONCLUSION

We have demonstrated that strong pumping of a long vapor cell creates a differential in the refractive index that will act as a gradient refractive index lens. Then when a broadband probe field is counterpropagated through the cell, only the portion of the probe near the dispersionless wavelength will freely propagate, while the rest of the frequencies will be refracted away from the detector. This technique could be used in other atomic vapors to experimentally verify the frequency of zeros in the resonant refractive index.

These dispersionless wavelengths are important for observing collective effects in long cells. Therefore the dispersionless wavelength may be useful for coherent collective control experiments in the future to avoid issues with dispersion.

[1] B. Arora, M. S. Safronova, and C. W. Clark, Phys. Rev. A **84**, 043401 (2011).

[2] L. J. LeBlanc and J. H. Thywissen, Phys. Rev. A **75**, 053612 (2007).

[3] C. D. Herold, V. D. Vaidya, X. Li, S. L. Rolston, J. V. Porto, and M. S. Safronova, Phys. Rev. Lett. **109**, 243003 (2012).

[4] N. Lundblad, M. Schlosser, and J. V. Porto, Phys. Rev. A **81**, 031611 (2010).

[5] A. A. Svidzinsky, L. Q. Yuan, and M. O. Scully, Phys. Rev. X **3**, 041001 (2013).

[6] P. R. Hemmer, N. P. Bigelow, D. P. Katz, M. S. Shahriar, L. DeSalvo, and R. Bonifacio, Phys. Rev. Lett. **77**, 1468 (1996).

[7] J. Keaveney, A. Sargsyan, U. Krohn, I. G. Hughes, D. Sarkisyan, and C. S. Adams, Phys. Rev. Lett. **108**, 173601 (2012).

[8] J. Keaveney, I. G. Hughes, A. Sargsyan, D. Sarkisyan, and C. S. Adams, Phys. Rev. Lett. **109**, 233001 (2012).

[9] R. H. Leonard, A. J. Fallon, C. A. Sackett, and M. S. Safronova, Phys. Rev. A **92**, 052501 (2015).

[10] C. O'Brien, P. M. Anisimov, Y. Rostovtsev, and O. Kocharovskaya, Phys. Rev. A **84**, 063835 (2011).

[11] B. W. Shore, *The Theory of Coherent Atomic Excitation* (Wiley, New York, 1990).

[12] M. S. Safronova and U. I. Safronova, Phys. Rev. A **83**, 052508 (2011).

[13] C. O'Brien and M. O. Scully, J. Mod. Opt. **63**, 27 (2016).

[14] A. Sharma, D. V. Kumar, and A. K. Ghatak, Appl. Opt. **21**, 984 (1982).

[15] A. F. Molisch and B. P. Oehry, *Radiation Trapping in Atomic Vapours* (Clarendon Press, New York, 1998).